Vertical Extrusion Cryo(bio)printing for Anisotropic Tissue Manufacturing

Zeyu Luo, Guosheng Tang, Hossein Ravanbakhsh, Wanlu Li, Mian Wang, Xiao Kuang, Carlos Ezio Garciamendez-Mijares, Liming Lian, Sili Yi, Junlong Liao, Maobin Xie, Jie Guo, Zongke Zhou, and Yu Shrike Zhang*

Due to the poor mechanical properties of many hydrogel bioinks, conventional 3D extrusion bioprinting is usually conducted based on the *X–Y* plane, where the deposited layers are stacked in the *Z*-direction with or without the support of prior layers. Herein, a technique is reported, taking advantage of a cryoprotective bioink to enable direct extrusion bioprinting in the vertical direction in the presence of cells, using a freezing plate with precise temperature control. Of interest, vertical 3D cryo-bioprinting concurrently allows the user to create freestanding filamentous constructs containing interconnected, anisotropic microchannels featuring gradient sizes aligned in the vertical direction, also associated with enhanced mechanical performances. Skeletal myoblasts within the 3D-cryo-bioprinted hydrogel constructs show enhanced cell viability, spreading, and alignment, compared to the same cells in the standard hydrogel constructs. This method is further extended to a multimaterial format, finding potential applications in interface tissue engineering, such as creation of the muscle–tendon unit and the muscle–microvascular unit. The unique vertical 3D cryo-bioprinting technique presented here suggests improvements in robustness and versatility to engineer certain tissue types especially those anisotropic in nature, and may extend broad utilities in tissue engineering, regenerative medicine, drug discovery, and personalized therapeutics.

1. Introduction

The 3D bioprinting technology has attracted increasing attention in tissue fabrication over the past couple decades.[1–4] As arguably the most common technique, conventional 3D extrusion bioprinting is mainly used for constructing volumetric structures in a layer-wise manner.[5] Although the layer-by-layer bioprinting method is functional in majority of the cases,[6] there are limitations associated with creating anisotropic tissues, such as muscle fibers[7,8] and nerve fibers[9] that heavily rely on cellular alignment for their physiologies. Therefore, developing a versatile strategy that allows convenient 3D bioprinting synergized with simultaneous generation of structural anisotropy is essential for these applications.

Numerous studies have shown that porous hydrogel scaffolds can potentially enhance cell spreading and proliferation.[10,11] In particular, ice-templating, one of the most widely utilized techniques for the fabrication of materials with anisotropic microchannels, allows control over pore morphologies by controlling directional ice formation in a suspension of solute(s).[12–15] During the freezing process, ice crystals form and propagate through a set direction within the biomaterial solution. When the construct cross-links and thaws, the melted ice crystals form interconnected anisotropic microchannels within the scaffold. Importantly, previous studies have clearly demonstrated that the presence of anisotropic microchannels enhances

Z. Luo, G. Tang, H. Ravanbakhsh, W. Li, M. Wang, X. Kuang,
C. E. Garciamendez-Mijares, L. Lian, S. Yi, J. Liao, M. Xie, J. Guo,
Y. S. Zhang
Division of Engineering in Medicine
Department of Medicine
Brigham and Women's Hospital
Harvard Medical School
Cambridge, MA 02139, USA
E-mail: yszhang@research.bwh.harvard.edu
Z. Luo, Z. Zhou
Department of Orthopedics
West China Hospital/West China School of Medicine
Sichuan University
Chengdu 610041, P. R. China

G. Tang
NMPA and Guangdong Key Laboratory of Molecular Target & Clinical
Pharmacology
State Key Laboratory of Respiratory Disease
School of Pharmaceutical Sciences
The Fifth Affiliated Hospital
Guangzhou Medical University
Guangzhou 511436, P. R. China
H. Ravanbakhsh
Department of Mechanical Engineering
McGill University
Montreal, QC H3A0C3, Canada

2108931 (1 of 13)

**ADVANCED
SCIENCE NEWS**
www.advancedsciencenews.com

**ADVANCED
MATERIALS**
www.advmat.de

alignment of postseeded cells.[16,17] However, the freezing process, including directional freezing, of the biomaterials will inevitably decrease viability of encapsulated cells. To this end, it is necessary to combine the biomaterials with cryoprotective agents (CPAs) to increase cell viability during and after the ice-templating process.

Dimethyl sulfoxide (DMSO) is one of the most widely used CPAs that can minimize damage on the cell membranes by hindering the intracellular and extracellular ice crystallization under cryogenic conditions.[18] Saccharides have also been widely used as naturally derived cryoprotectants.[19] Due to their high molecular weights, saccharides do not penetrate the cell membranes and would merely act on the extracellular surfaces of cells. Furthermore, saccharides can reduce the amount of water in contact with cells by increasing the osmolarity of the extracellular medium.[18–20] Among various disaccharides, melezitose has shown promising cryoprotective effects;[20] therefore, it was chosen, either to act alone or in combination with DMSO, as the CPA.

Here, we report an enabling technique that was largely unexplored before, termed vertical 3D extrusion cryo-bioprinting, that combines 3D extrusion bioprinting and ice-templating methods to fabricate vertical, high-aspect-ratio, cell-laden hydrogel constructs with interconnected, anisotropic, gradient microchannels. As schematically briefed in **Figure 1**A, a gelatin methacryloyl (GelMA)-based hydrogel scaffold containing anisotropic microchannels could be formed after ice-templating. The vertical 3D cryo-bioprinting technique was shown for its ability to produce pillar arrays (Figure 1B), filaments at oblique angles (Figure 1C), multimaterial filaments (Figure 1D), and scaffolds with arrays of heterogeneous filaments (Figure 1E). As proof-of-concept demonstrations, we further utilized the vertical 3D cryo-bioprinting technique to fabricate the muscle–tendon unit (MTU) (Figure 1F) with C2C12 myoblasts and NIH/3T3 fibroblasts, as well as the muscle–microvascular unit (MMVU) (Figure 1G) with C2C12 myoblasts and human umbilical vein endothelial cells (HUVECs). Our results indicated that the bioink, consisting of GelMA and CPAs, could be effectively used in vertical 3D cryo-bioprinting to enable cell encapsulation at high viability levels. With the help of the interconnected, anisotropic, gradient microchannels formed by directional freezing during the vertical 3D cryo-bioprinting process, the desired cellular alignments were also realized. These fabricated tissue constructs may find a plethora of applications in muscular tissue engineering and beyond.

2. Results and Discussion

A thermoelectric cooler was used to precisely control the temperature on the substrate surface via adjusting the input voltage (**Figure 2**A). Using polydimethylsiloxane molds, the 7.5% (w/v for all expressions unless otherwise indicated) rhodamine B-conjugated GelMA solution was directionally frozen using −20 °C as the substrate temperature. The samples were then exposed to UV light to fully cross-link. During the ice-templating process, lamellar ice crystals would start to grow from the substrate surface throughout the GelMA construct vertically.[12,17,21] To confirm, the scaffolds were subsequently sliced into four

pieces with a thickness of 1 mm each and imaged using a fluorescence microscope at the cross-sections. Honeycomb-like networks of microchannels at the cross-sections were apparent after the directional ice-templating process, showing gradient pore sizes across the height of the construct (Figure 2B and Movies S1 and S2 (Supporting Information)).[22,23] In previous studies, it was also found that the temperature gradient can control the diameter of the microchannels, which is consistent with the current study.[13–15] Following the measurements of the microchannel sizes directly from the fluorescence microscopy images, it was quantified that the diameter of the microchannels increased from 70.68 ± 15.64 to 513.63 ± 39.88 µm along the ice-templating direction from bottom to top (Figure 2C and Figure S1 (Supporting Information)). Under the pressure of the lamellar ice crystals during the directional freezing process, the GelMA chains self-coalesced and became separated from the initial homogeneous phase, which in turn formed the micrometer-scale aligned porous microchannels, as revealed also in the sagittal views (Figure 2D,E and Figure S1 (Supporting Information)).[22]

Through the diffusion assay using a blue dextran solution, the interconnectivity of the microchannels of the ice-templated GelMA hydrogel was examined (Figure S2, Supporting Information). It was observed that the blue dextran solution could easily transport through the directionally frozen GelMA hydrogel disk but could not readily permeate the control GelMA scaffolds. The substrate temperature was further adjusted from −5 to −20 °C to study the effect of substrate temperature on the pore size of the resulting scaffolds (Figure 2F). As the substrate temperature was decreased from −5 to −20 °C, the pore size in the bottom layer decreased from 184.81 ± 26.19 to 23.80 ± 5.0 µm (Figure 2G). The transparency of the GelMA scaffolds at different freezing temperatures was also compared. As the freezing temperature was reduced, the transparency of the scaffolds gradually decreased as well (Figure S3, Supporting Information), due to the formation of denser porous structures inside. In addition, we investigated the influence of GelMA concentration on the diameter of the microchannels, wherein as the concentration of GelMA was increased, the microchannel size decreased (Figure S4, Supporting Information).

Directional ice-templating results in increased local concentrations of GelMA surrounding the ice crystals, leading to the formation of anisotropic microchannels.[22,23] The mechanical properties of the hydrogel constructs with anisotropic microchannels were investigated with compressive and tensile testing. The 7.5% GelMA hydrogels prepared via directional freezing showed unique anisotropic mechanical properties (Figure 2H–K). It was found that when 7.5% GelMA was directionally frozen at −20 °C, the compressive modulus parallel to the freezing direction of the scaffolds (151.56 ± 1.56 kPa) increased significantly than that perpendicular to the freezing direction (64.32 ± 3.47kPa), though both much larger than that of the control, isotropic samples (3.88 ± 0.31 kPa) (Figure 2H,I). Also, the tensile modulus parallel to the freezing direction of the directionally frozen GelMA scaffolds at −20 °C increased to 196.40 ± 3.19 kPa, which was significantly higher than that perpendicular to the freezing direction (125.30 ± 3.18 kPa) and was almost 55 times higher than that of the control, isotropic samples (3.61 ± 0.29 kPa) (Figure 2J,K). Together, such an

**ADVANCED
SCIENCE NEWS**

www.advancedsciencenews.com
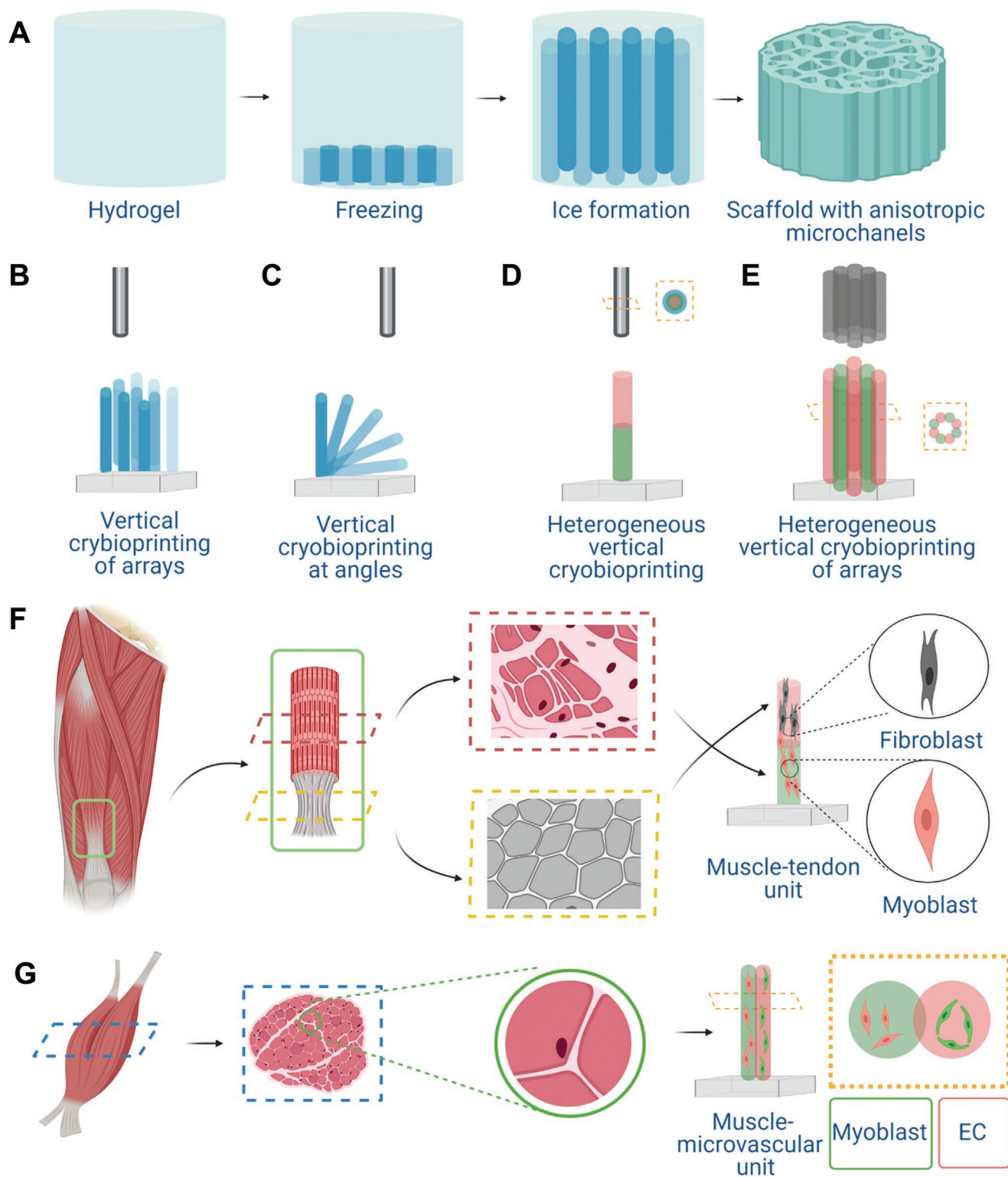
**ADVANCED
MATERIALS**

www.advmat.de

Figure 1. Schematic illustrations of vertical 3D cryo(bio)printing and its application in muscular tissue engineering. A) The GelMA-based hydrogel, when subjected to directional freezing, forms interconnected gradient and anisotropic microchannels along the vertical axis. B) Vertical 3D cryo(bio)printing of hydrogel filament arrays. C) Vertical 3D cryo(bio)printing of hydrogel filaments of different angles. D) Multimaterial vertical 3D cryo(bio)printing of a single hydrogel filament. E) Multimaterial vertical 3D cryo(bio)printing of hydrogel filament array. F,G) Vertical 3D cryo-bioprinting for fabricating the MTU (F) and the MMVU (G).
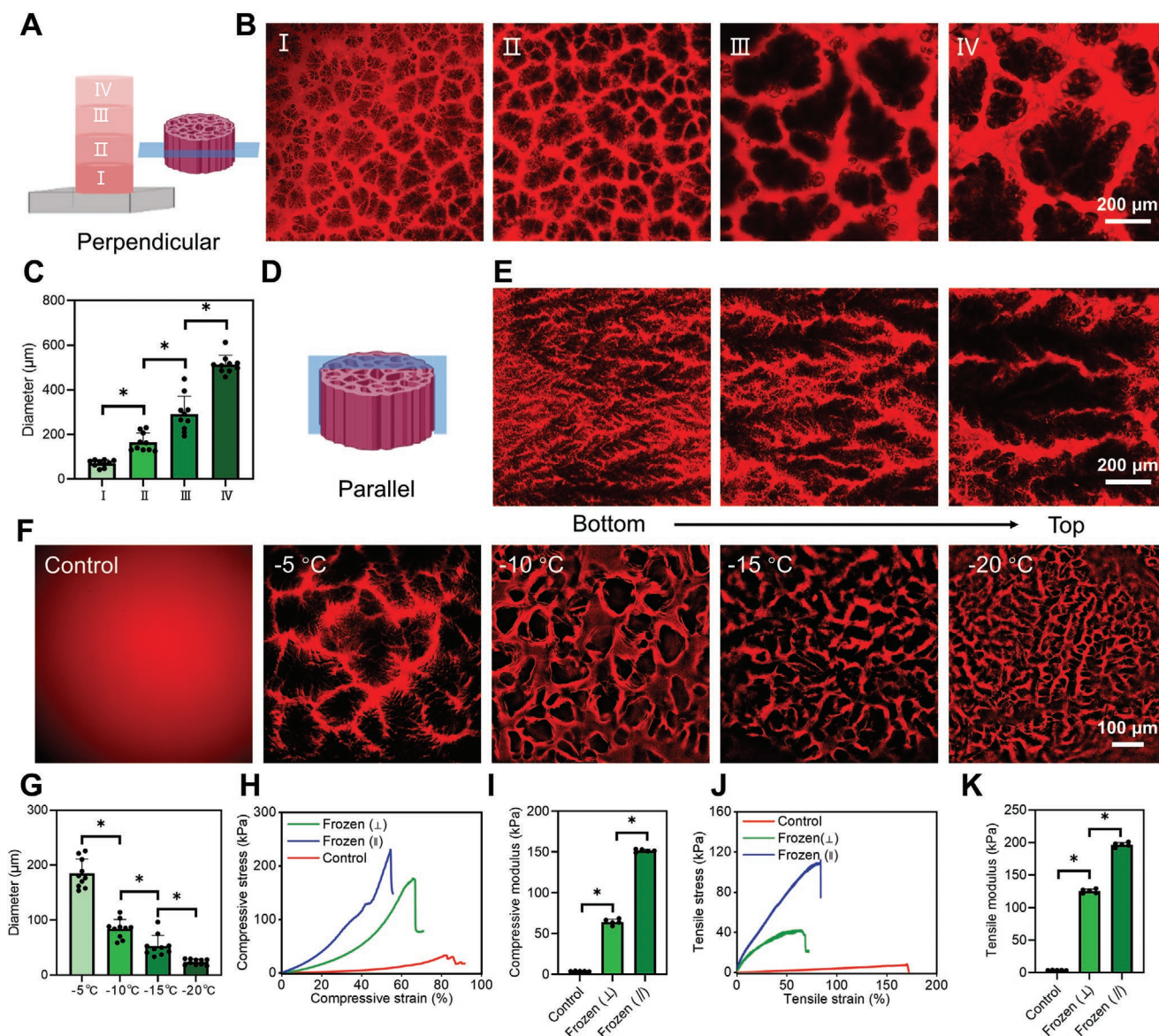
Figure 2. Characterizations of the vertically ice-templated 7.5% GelMA constructs. A) Schematic of the vertically ice-templated GelMA construct, and the cross-section showing microchannels perpendicular to the freezing direction. According to the temperature gradient, the construct was sliced into 4 pieces (I, II, III, and IV). B) Fluorescence microscopy images showing the effect of temperature gradient on the microchannel sizes in the GelMA (7.5%) construct, prelabeled with rhodamine B. C) The corresponding quantification results of microchannel diameters at the different temperature layers. D) Schematic showing the microchannels along the freezing direction in the vertically ice-templated GelMA construct. E) Fluorescence microscopy image showing a gradient scaffold with microchannel width increasing from bottom (left) to top (right). F) Fluorescence microscopy images showing the diameter of the microchannels in the scaffolds decreasing with the freezing-plate temperature changing from −5 to −20 °C. G) The corresponding quantification results of the diameters of the microchannels. H) Compressive stress–strain curves and I) compressive moduli of the GelMA hydrogels directionally frozen at −20 °C. J) Tensile stress–strain curves and K) tensile moduli of GelMA hydrogels directionally frozen at −20 °C. The control samples were GelMA hydrogels undergoing no freezing steps (*$p < 0.05$).

ice-templating method could increase the local concentrations of GelMA chains with simultaneously enhanced anisotropic microchannels and mechanical properties in the GelMA hydrogel constructs.[22,23]

Figure 3A schematically illustrates the vertical cryoprinting process of a GelMA pillar. The bioink is extruded onto the freezing plate through the nozzle to produce a vertically oriented structure. Although the printing of such vertical structures may also be possible when using an ambient freezing chamber,[24] anisotropic microchannels would not form as in our case with the use of the freezing plate at the bottom. In addition, an ambient freezing chamber may cause freezing of the bioink at the cartridge, potentially making the printing process difficult. In our setup, the temperature gradually decreases along the vertical direction from the bottom to the top. By adjusting the input voltage of the freezing plate, we were able to accurately control the freezing plate temperature from −5 to −30 °C (Figure 3B), which accordingly, would affect
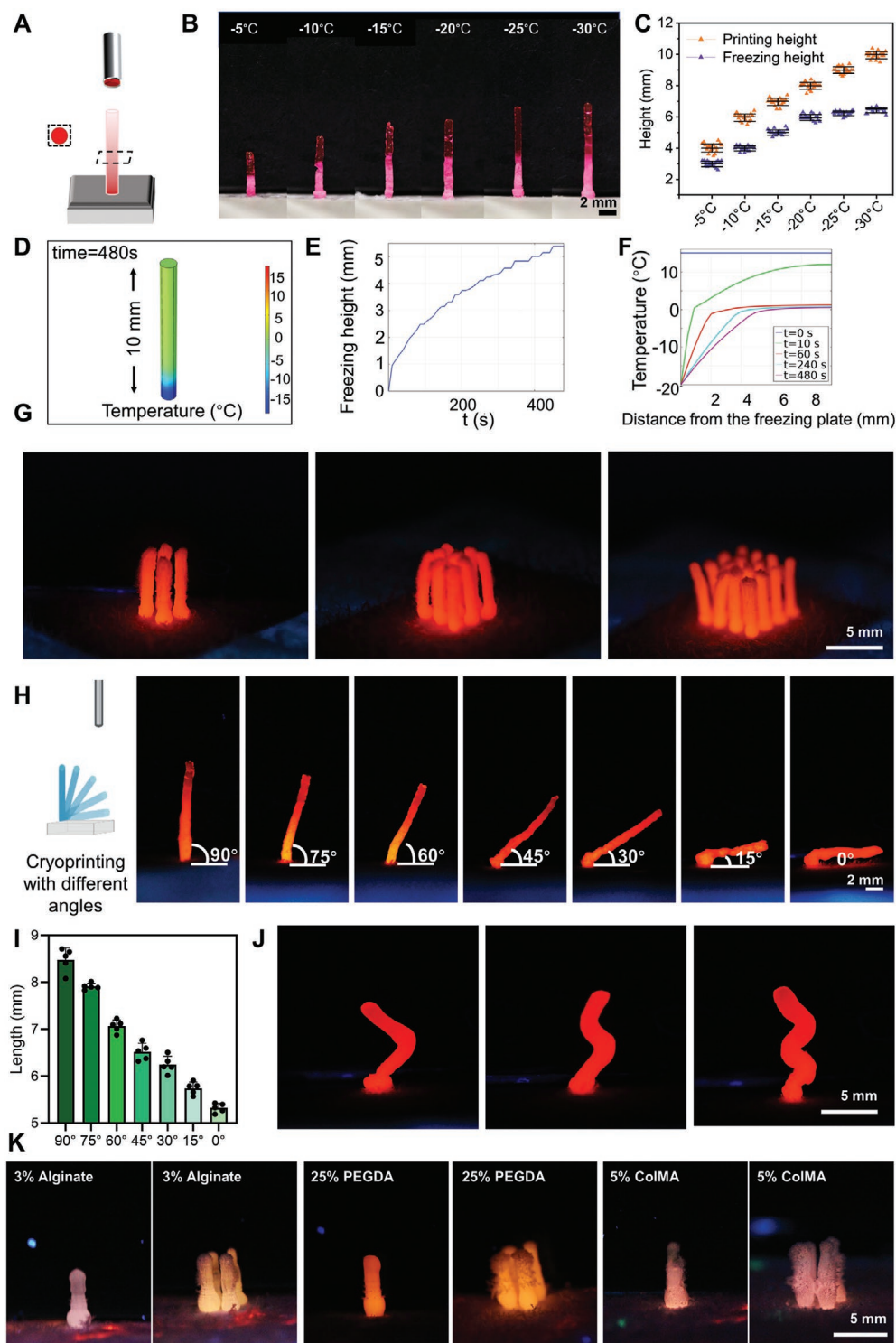
Figure 3. Vertical 3D cryoprinting experimental and simulation results. A) Schematic showing the vertical 3D cryoprinting process. B) Photographs showing changes in the freezing and printing heights in cryoprinted 7.5% GelMA pillars as a function of the freezing plate temperature. C) The corresponding quantification results of the vertical freezing and printing heights. D) Simulated temperature gradient in a vertical structure at 480 s after cryoprinting. E) Simulated height of freezing in the cryoprinted structure gradually increasing with time. F) Simulated temperature distributions throughout the vertically cryoprinted constructs decrease gradually over time. G) Fluorescence photographs showing vertically cryoprinted GelMA bioink arrays containing 4, 9, and 16 pillars. H) Fluorescence photographs showing vertically cryoprinted GelMA constructs at different angles. I) The corresponding quantification results of the printable lengths at different angles. J) Fluorescence photographs showing cryoprinted sophisticated GelMA structures. K) Fluorescence photographs showing vertically cryoprinted 2-by-2 pillar arrays by bioinks without thermogelling properties (3% alginate, 25% PEGDA, and 5% ColMA).

the freezing speed and the printing speed. Of note, the bioink mixture is a eutectic system, and due to its colligative properties, it may have a freezing point of lower than 0 °C depending on the type and concentration of its components. The effect of gelatin concentration on the freezing point has been previously investigated in another study.[25] Accordingly, for the case of 7.5% GelMA that we used primarily as the bioink, the freezing point was estimated at –0.45 °C (Figure S5, Supporting Information). As shown in Figure 3B, when the freezing plate temperature was reduced, the heights of freezing and cryoprinting of GelMA constructs both increased. When the temperature of the freezing plate was –5 °C, the average freezing height of the pillar was 2.99 ± 0.17 mm. As the temperature declined to –30 °C, the average height of freezing increased to 6.43 ± 0.15 mm (Figure 3C). In addition, to explore how ambient temperature might affect the cryoprinting process, we further made an enclosure to maintain the ambient temperature at 4 °C instead of the room temperature otherwise used. We found that there was no noticeable difference in the height of freezing with or without a chamber (Figure S6, Supporting Information). Similarly, the heights of cryoprinting increased when lower temperatures were used for the freezing plate. We also assessed the cryoprinting performances of GelMA with different concentrations (2.5%, 5%, 7.5%, 10%, 12.5%, and 15%) on the freezing plate (–20 °C) (Figure S7, Supporting Information).

Since the bioink for vertical 3D cryoprinting freezes immediately after contacting with the freezing plate, those with very low viscoelasticity values, such as the 2.5% GelMA bioink, were conveniently cryoprinted vertically (Figure S7, Supporting Information), which would be almost impossible in conventional extrusion bioprinting without freezing for a bioink containing this low polymer concentration. Different sizes of the nozzles (18G, 20G, 21G, 22G, 23G, and 25G) were also evaluated for vertical 3D cryoprinting (Figure S8, Supporting Information). We successfully tuned the diameter of the cryoprinted GelMA pillar structures, where it was further observed that the nozzle diameter did not seem to affect their freezing heights although the printing heights suggested a slightly decreasing trend when the nozzle size was reduced. It was possibly because as the nozzle size was decreased, the GelMA structure was more likely to break during the printing process toward the top and therefore would cause a decreasing height of the cryoprinted pillar. The swelling ratio of the cryoprinted structures was also measured, and the swelling ratio was ≈12% at 1 day after printing (Figure S9, Supporting Information).

COMSOL Multiphysics was used to simulate phase-changing heat transfer in the vertically cryoprinted structures. Figure 3D and Movie S3 (Supporting Information) show the simulation of heat transfer during the 480 s of vertical cryoprinting. As the bioink is in direct contact with the freezing plate (–20 °C), the heat transfers from the bioink and it gradually freezes upward. It is worth mentioning that the cooling rate in the bioink decreased as the construct height was increased; the higher the vertical structure, the longer it took for the sample to freeze (Figure 3E). In Figure 3F, the predicted temperatures over the height of the construct at different time points are plotted. The results portrayed that the height of freezing of the bioink construct nicely matched those of the simulation model, which is an indicator of synergy between simulation and experimental

results. Specifically, as illustrated in Figure S10 (Supporting Information), we repeated the heat-transfer simulation for 5-mm pillars to directly compare the results with experimental data. When the 5-mm pillars were vertically cryoprinted, the freezing height reached 1.9 mm in 36 s (Movie S4, Supporting Information), which was close to the value obtained from the simulation, i.e., 1.7 mm (Figure S10, Supporting Information). When 10-mm vertical pillars were cryoprinted at –20 °C (Figure 3B), the ultimate freezing height reached roughly 5 mm, which was also very close to the simulation results in Figure 3E, further providing good agreement between experimental data and simulation results regardless of the pillar height.

Vertical GelMA pillar arrays, featuring 2-by-2, 3-by-3, and 4-by-4 filaments, were successfully cryoprinted to further demonstrate the capability of the vertical 3D-cryoprinting technique (Figure 3G and Figure S11 and Movie S4 (Supporting Information)). In addition, oblique GelMA structures cryoprinted at a wide range of angles, from 90° to close to 0° varying every 15°, were obtained at –20 °C of the freezing plate (Figure 3H and Figure S12 (Supporting Information)). We also measured the length of the cryoprinted structures and concluded that the printable length was dependent on the angle of the pillar (Figure 3I). The printable length of the construct at 90° was 8.48 ± 0.25 mm, consistent with our previous results, while it was 5.32 ± 0.08 mm for 0°. The direction and diameter of the microchannels of the cryoprinted vertical and 45° filaments were also compared, where no significant differences were found between the samples in both of these parameters (Figure S13, Supporting Information). Although nanocomposite hydrogels can be extrusion-printed in 3D freeform as well as using vat polymerization-based method,[26,27] our vertical 3D-cryoprinting technique was more convenient in producing various vertical GelMA structures (Figure 3J and Figures S14 and S15 (Supporting Information)) and that were spiral (Figure S16, Supporting Information), without necessitating bioink or instrument complexity. In addition to cryoprinting GelMA vertically, bioinks without thermogelling properties (3% alginate, 25% poly(ethylene glycol)-diacrylate (PEGDA), and 5% collagen methacryloyl (ColMA)) were also successfully cryoprinted in the vertical direction as single pillars and as 2-by-2 pillar arrays (Figure 3K and Figure S17 (Supporting Information)).

Another unique feature of vertical 3D cryoprinting is the ability to create sophisticated vertical structures such as those hollow or/and multimaterial in nature. We first utilized coaxial nozzles to extrude the GelMA bioink containing green fluorescent microbeads in the sheath layer, and cryoprinted hollow vertical structures of different core diameters with the help of 21G, 23G, and 25G inner needles, where the outer layer of the nozzles was fixed at 18G (**Figure 4**A and Figure S18 (Supporting Information)). The hollow core diameters of the resulting constructs were measured using the fluorescence microscopic images. As shown in Figure 4D and Figure S19 (Supporting Information), the core diameters were 241.94 ± 12.88, 148.69 ± 8.63, and 119.99 ± 8.08 µm, respectively, for 21G, 23G, and 25G inner needles.

In addition, core–shell vertical constructs made of multiple materials could be cryoprinted when two different bioinks were loaded in the core and shell during the fabrication
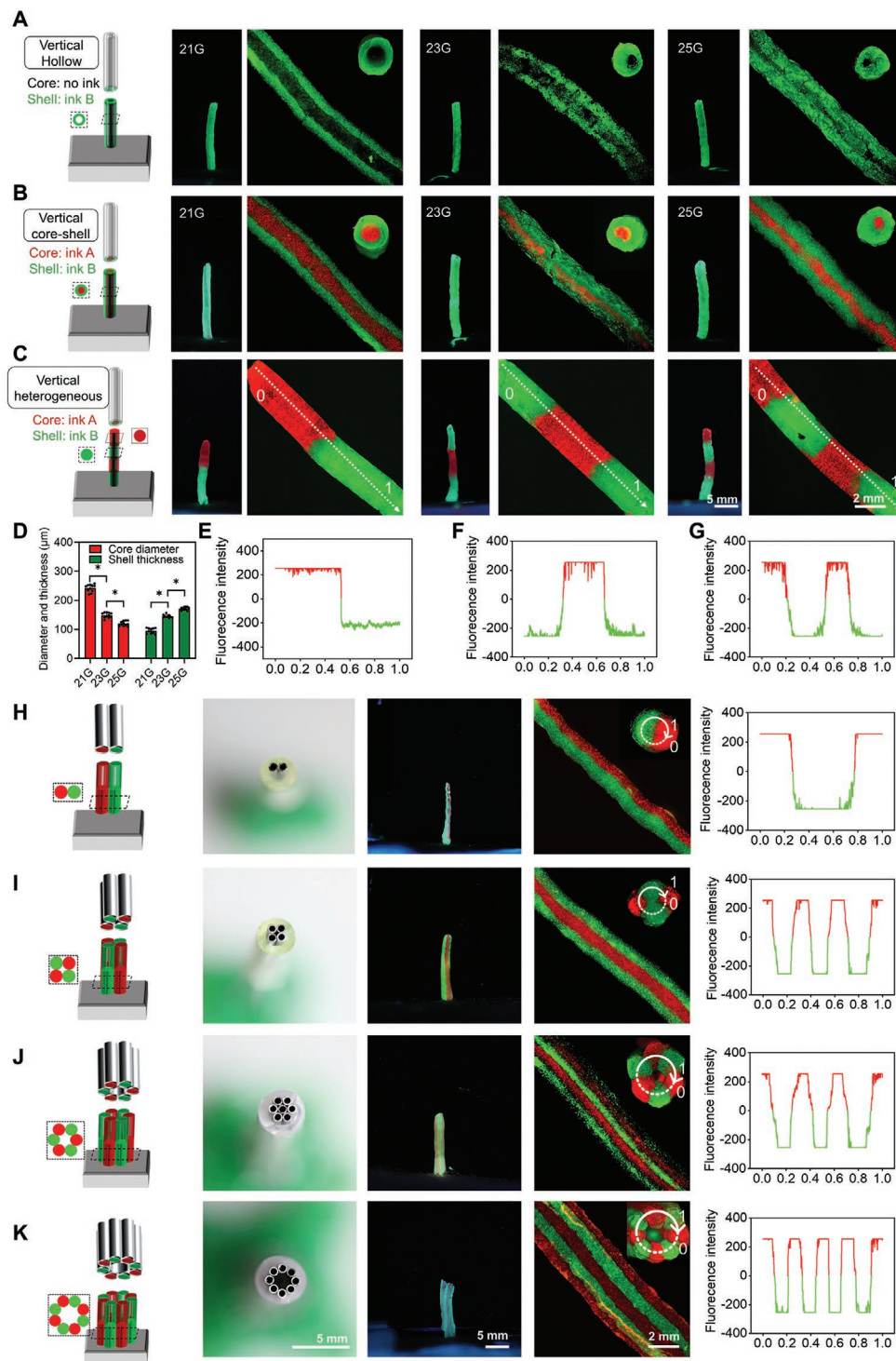
Figure 4. Vertical 3D cryoprinting of various single- and multimaterial GelMA constructs. A) Schematic and fluorescence images showing vertically cryoprinted hollow constructs consisting of different wall thicknesses, fabricated with coaxial nozzles containing varying inner needle sizes. B) Schematic and fluorescence images showing vertically cryoprinted multimaterial core–shell structures, fabricated with coaxial nozzles with varying inner needle sizes. C) Schematic and fluorescence images showing vertically cryoprinted multimaterial programmable heterogeneous solid structures fabricated with a coaxial nozzle. D) Quantification results of the wall thicknesses and the core sizes in vertically cryoprinted hollow structures shown in (A,B). E–G) Fluorescence intensity profiles of vertically cryoprinted heterogeneous solid structures shown in (C). For the lines in the plots, the starting point of each line is 0 and the end point is 1, as indicated in in the lines shown in the corresponding microscopy images. H–K) Schematics, photographs, and fluorescence images showing vertically cryoprinted multicompartmental structures, fabricated with nozzles with varying amounts of bundled channels. For the lines in the plots, the starting point of each line is 0 and the end point is 1, as indicated in the circles shown in the corresponding microscopy images (*$p < 0.05$).

process (Figure 4B and Figure S20 (Supporting Information)). Although creating fibers with multilayer structures has been previously investigated,[28–31] our unique vertical cryoprinting method introduces additional flexibility to their production with enhanced structural controls. The shell thicknesses of the cryoprinted vertical core–shell structures were measured at 95.18 ± 9.33, 145.36 ± 5.20, and 171.76 ± 5.24 μm, respectively, for 21G, 23G, and 25G inner needles (Figure 4D). More interestingly, a programmable distribution of the multiple materials along the vertical direction of the solid filaments could be achieved by periodically switching the core and shell channels ON/OFF (Figure 4C and Figure S21 (Supporting Information)). The corresponding fluorescence intensity profiles indicated that the various components within a given cryoprinted vertical structure were physically well-separated (Figure 4E–G).

Beyond vertical cryoprinting of hollow, core–shell, and heterogeneous structures, we also designed a group of nozzles containing 1, 2, 4, 6, and 8 bundled channels for parallel vertical 3D cryoprinting (Figure 4H–K and Figure S22 (Supporting Information)).[32–35] The red and green colors represent different bioinks extruded from the different channels. Through this enabling nozzle system, vertical structures containing up to 8 bioinks were able to be fabricated. Similarly, the fluorescence intensity profiles demonstrated the well-defined multimaterial compositions in the corresponding vertically cryoprinted constructs. Nevertheless, because the structure undergoes gradient cooling, the part near the cold plate freezes first and the part at the top freezes later, and therefore the connections in the bundles might be different among different sections of the bundle. This point may require further exploration.

One exceptional feature in directional ice-templating within hydrogel scaffolds is the formation of anisotropic microchannels possibly with gradient sizes, which facilitate proper cell growth and designed alignment.[12,23,36] As previously stated, in vertical 3D cryoprinting, the cooling rate changes in relation to the height of the sample deposited; thus, dissimilar ice crystals are formed, leading to the formation of microchannels with graded alignments and sizes. On the other hand, ice crystals can also damage cell membranes resulting in poor cell viability.[37] Maintaining cell viability during the ice-templating process is, therefore, a key factor in designing bioinks for cell-laden vertical cryoprinting, i.e., vertical cryo-bioprinting.

The C2C12-myoblast-laden cryo-bioprinted samples containing DMSO and melezitose were subjected to Live/Dead assays on days 1, 3, and 7. The 7.5% GelMA bioinks containing different concentrations (5%, 10%, and 15%) of DMSO were initially used to gain understanding on its cryoprotectant effect. As revealed in Figure S23 (Supporting Information), the optimum concentration of DMSO was found at 10% for maximizing cell viability in the absence of the saccharide. GelMA bioinks containing different concentrations (4%, 8%, and 12%) of melezitose in the absence of DMSO were separately used for optimizing the melezitose effect. The results suggested that 8% melezitose could lead to the highest cell viability, and further increasing the melezitose concentration had no significant benefit (Figure S24, Supporting Information). Figure S25 (Supporting Information) shows a representative set of Live/Dead images of the cells cryopreserved in 7.5% GelMA alone, or with different DMSO and melezitose concentrations. The

CPA-free control group generally suggested the lowest cell viability values across the 7 days of culture, while the samples containing a mix of DMSO and melezitose showed the highest cell viability. Therefore, the GelMA bioink combined with 8% melezitose and 10% DMSO was determined as the optimum formulation for cell-laden vertical cryo-bioprinting, and used in the following cellular experiments. Of note, the viability of the C2C12 cells at day 1 was ≈60% in the presence of both the optimal DMSO (10%) (Figure S23, Supporting Information) and the optimal melezitose (8%) (Figure S24, Supporting Information) conditions. However, in Figure S25 (Supporting Information) also under similar conditions, the viability of the C2C12 cells at day 1 was observed at 80%. Such an inconsistency might be caused by the different passage numbers of the different batches of cells or other inevitable differences in the experiment processes. While we felt that these inconsistencies were within acceptable error ranges, we always had control groups in these experiments to maximize the validity of the results.

Furthermore, the more fragile human mesenchymal stem cells were also evaluated to verify the cryo-bioprinting method and cryopreservation efficacy using the optimum bioink formulation. Figure S26 (Supporting Information) suggests that the cell viability was ≈79.2%, 84.5%, and 83.9% after 1, 7, and 14 days of culture following cryo-bioprinting, respectively. In a previous study, researchers bioprinted 3% alginate with osteoblast-like cells at −40 to −2 °C.[38] The results showed that cell viability was less than 40% when the temperature was lower than −20 °C.[38] Differently, in the current study, we illustrated that directional freezing in combination with cryo-bioprinting could generate anisotropic microchannels and induce the desired cell alignment, as we will show below, which has not been reported before.

We studied the cell viability in the frozen and unfrozen areas of the same vertically cryoprinted filament surrounding the junction point (**Figure 5**A). The unfrozen section was incorporated in this scenario with the aid through intentionally cryo-bioprinting a longer filament beyond the frozen height. It was clear that C2C12 cell viabilities in both frozen and unfrozen segments were 82% on day 1 (Figure 5B), proving that the cryoprotective bioink could effectively reduce the adverse effects of ice crystals on cell viability during the cryoprinting process. In addition, cell viability in the frozen segment was found to be higher than that in the unfrozen areas on days 3 and 7 (Figure 5B); on the 7th day, the cell viability in the frozen area was 94.01 ± 2.34%, which was 5% higher than that in the unfrozen area (88.90 ± 1.63%) (Figure 5B), although both were deemed decently high and sufficient for our cryo-bioprinting applications. The explanation for the lower viability in the unfrozen part might be the extended presence duration of DMSO at above-freezing temperature, or possibly the presence of microchannels in the frozen portion that served to enhance the cell growth after vertical cryo-bioprinting during the subsequent culture period.

The myotube spreading in the vertically 3D-cryo-bioprinted hydrogel scaffolds on days 1, 3, and 7 was examined to demonstrate the advantages of the gradient microchannel configuration (Figure 5C and Figure S27A (Supporting Information)), the timeline of which is widely used in literature for assessing
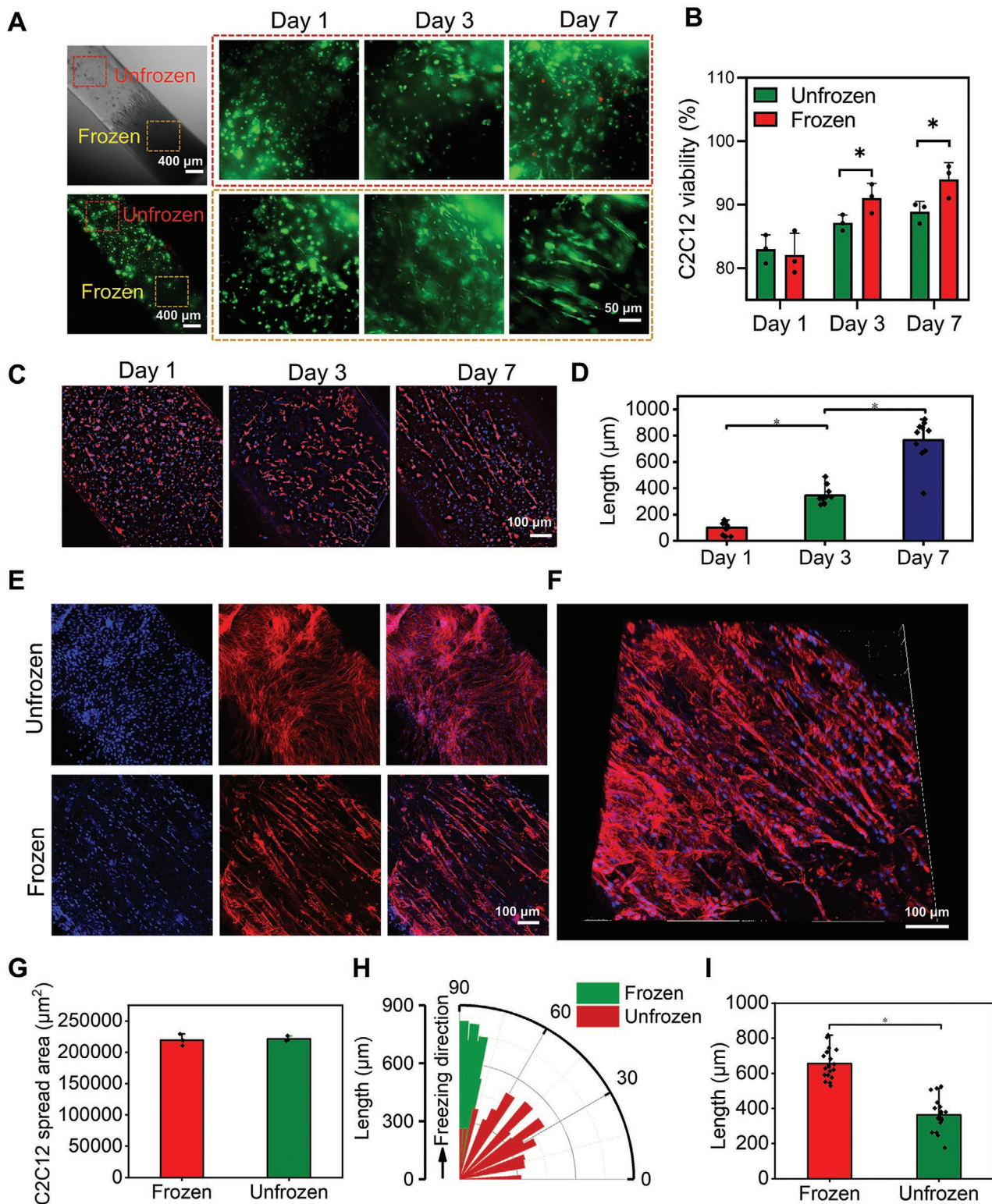
**ADVANCED
SCIENCE NEWS**
www.advancedsciencenews.com

**ADVANCED
MATERIALS**
www.advmat.de

Figure 5. Behavioral characterizations of C2C12 cells encapsulated in the vertically cryo-bioprinted GelMA constructs. A) Bright-field and fluorescence microscopy images showing viability of encapsulated C2C12 cells in the frozen and unfrozen areas in a single vertically cryo-bioprinted structure on days 1, 3, and 7 of culture. Live cells were stained in green and dead cells in red. B) The corresponding quantification results of cell viability. C) Fluorescence microscopy images showing myotube formation from days 1 to 7 in the frozen area of a vertically cryo-bioprinted structure. D) The corresponding quantification results of myotube lengths. E) Fluorescence microscopy images showing myotube formation in the frozen and unfrozen areas on day 7. F) Confocal reconstruction showing aligned myotubes in the frozen segment on day 7. G–I) The corresponding quantification results of myotube spreading areas (G), myotube angle distributions (H), and myotube lengths on day 7 (*$p < 0.05$) (I).

engineered muscular tissues.[39] We found that C2C12 cells could differentiate into well-aligned myotubes within these microchannels. The myotubes' length started from 100.39 ± 48.79 µm (per microscopic view) on day 1 and reached 636.36 ± 68.19 µm on day 7 (Figure 5D). Similarly, the cell spreading area gradually increased from 50 579.00 ± 1612.88 µm² (per microscopic view) to 80 227.66 ± 1460.71 µm² (Figure S27B, Supporting Information). The spreading of myotubes in the frozen and unfrozen areas of a single vertically cryo-bioprinted filament was compared (Figure 5E). The myotube alignment in the anisotropic microchannels in the frozen segment was further characterized via 3D reconstruction of the Z-stack images captured with confocal fluorescence microscope (Figure 5F). Movies S5 and S6 (Supporting Information) present videos of 3D reconstructions more clearly showing the myotube formation in the unfrozen and frozen zones, respectively. It was indicated that there was no significant difference in the spread areas of the myotubes in the two segments on day 7 of culture (Figure 5G). Compared with the random distribution of the myotubes in the unfrozen area, most of the myotubes in the frozen area were oriented perpendicular to the cross-section of the filament (Figure 5H), again confirming that the anisotropic microchannels within the frozen segment were able to support the alignment and fusion myoblasts. The anisotropic microchannels were also influential in the increase of the myotube length. Compared with myotube length in the unfrozen area, i.e., 363.19 ± 88.53 µm, their length in the frozen area significantly increased to 655.48 ± 83.04 µm (Figure 5I). It should be noted that other strategies, such as including fibers into bioinks to induce cell alignment and functions, have also been demonstrated before.[40–42] In comparison, our vertical cryo-bioprinting strategy could not only form the aligned microchannels to enhance cell alignment at the microscale but also allowed generation of macroscale aligned filaments. Moreover, the mechanical properties of the filaments would be significantly increased as well, in addition to the ability to cryogenically store these cryo-bioprinted vertical structures prior to their thawing and culture as needed under certain usage scenarios.

In muscular tissue engineering, one of the most challenging problems is the reconstruction of the MTU.[39,43] There have been previous studies on bioprinted muscle[44–46] or tendon[47] separately, but very few on employing cell-laden bioinks to create the MTU constructs through bioprinting, which still lacked localized topographical cues to allow necessary alignments.[39] The key part of MTU is the muscle–tendon junction, which transmits the contraction force of the muscle through the tendon to the skeletal system.[48] We took advantage of our vertical 3D cryo-bioprinting technique to propose a unique strategy for fabricating the muscle–tendon junction with preliminary biological characterizations. In this strategy, the junction was coincided with the frozen-to-unfrozen transition point of the vertically cryo-bioprinted filament, such that the myoblasts in the lower segment were highly aligned, while the fibroblasts less aligned with a junction in between, mimicking the natural structure (**Figure 6**A). Red and green fluorescent tracers were used to label NIH/3T3 fibroblasts and C2C12 myoblasts, respectively, to visualize the cell distributions in the vertically cryo-bioprinted MTU-like constructs (Figure 6B and

Figure S28 (Supporting Information)). Fluorescence images in Figure 6B clearly showed the junction between the muscle and tendon portions.

In addition, we used immunofluorescence to demonstrate the possible formation of the muscle–tendon junction, by labeling C2C12 and NIH/3T3 cells using anti-myosin heavy chain (MHC) and anti-collagen I antibodies, respectively (Figure 6C). The increase in the area of MHC staining on the muscle side from 1866.33 ± 626.06 to 24 278.33 ± 1927.53 µm² after 7 days of culture (Figure S29, Supporting Information) confirmed the formation of aligned myotubes. Similarly, on the tendon side, the increase in the area of collagen I from 1983.33 ± 368.46 to 26 266.00 ± 1221.51 µm² was evident (Figure S29, Supporting Information), suggesting that the fibroblasts were functional to secrete the main protein component of the tendon extracellular matrix (ECM). Moreover, the lengths of myotubes and fibroblasts gradually increased to 700.87 ± 56.34 and 494.61 ± 95.53 µm, respectively, during the 7 days of culture (Figure 6D). Most importantly, the fluorescence intensity profiles indicated that the C2C12 cells and the NIH/3T3 cells were tightly connected within the microchannels at the interface region, which indicated that the vertical 3D cryo-bioprinting method was effective in the reconstruction of a preliminary muscle–tendon junction model (Figure 6E). The orientations of the C2C12 cells and the NIH/3T3 cells were also assessed. The C2C12 cells in the lower area of the filament were oriented perpendicular to the cross-section of the filament, and the NIH/3T3 cells were less aligned in the upper region of the filament, which is close to the natural structure of the MTU (Figure 6F).

On the other hand, the skeletal muscle is known to be highly vascularized.[49] Microvasculature in the skeletal muscle is essential for supplying nutrients and oxygen as well as metabolic waste removal.[7,49] Tissue survival depends on oxygen supply, which is limited to a diffusion distance of up to ≈200–300 µm from the supplying blood vessel.[50] Researchers have embedded endothelial cells and myoblasts into hydrogel scaffolds to form vascularized grafts.[50–52] However, bioprinting of microvascularized skeletal muscle tissues still remains challenging in general.[7] Accordingly, the interconnected, aligned microchannels in the vertically cryo-bioprinted hydrogel scaffolds were also exploited to fabricate the MMVU (Figure 6G). We used red and green fluorescent tracers to, respectively, label HUVECs and C2C12 cells, and conducted vertical 3D cryo-bioprinting using a parallel, two-channel nozzle configuration (Figure 6H). Fluorescence images showed a distinct interface between the muscular and vascular filaments (Figure 6H).

Anti-MHC and anti-cluster of differentiation 31 (CD31) antibodies were then used to immunologically stain C2C12 cells and HUVECs, respectively (Figure 6I). The HUVECs formed a dense microvascular network within the microchannels in the filament they were embedded in during vertical cryo-bioprinting, over the 7 days of culture, which were well-aligned with the adjacent myofibers in the parallel filament. It was also quantified that the average length of the microvessels reached 217.54 ± 28.14 µm at day 7 of culture, and their areas increased from 1538.00 ± 409.79 to 14 748.33 ± 792.04 µm² from days 1 to 7 (Figure S29, Supporting Information). The myotube length increased from 15.01 ± 5.56 µm on day 1 to 591.36 ± 48.48 µm on
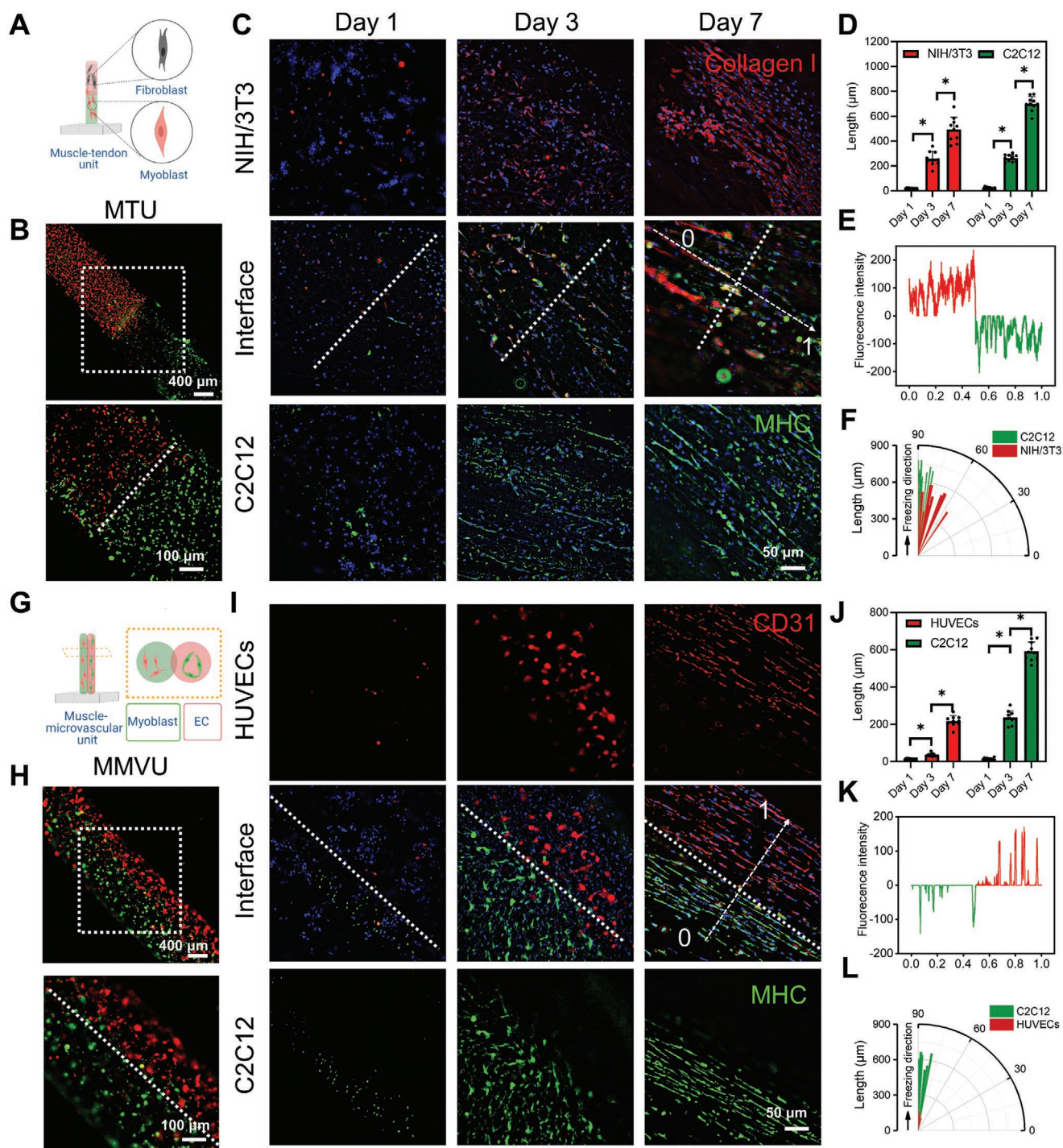
Figure 6. MTU and MMVU fabricated via vertical 3D cryo-bioprinting. A) Schematic of the MTU reconstructed by C2C12 myoblasts and NIH/3T3 fibroblasts. B) C2C12 (green) and NIH/3T3 (red) cells labeled with fluorescence tracers and vertically cryo-bioprinted as a MTU model on day 7. C) Fluorescence microscopy images showing MTU formation from days 1 to 7 after vertical 3D cryo-bioprinting. D–F) Quantification results of cell lengths from days 1 to 7 (D), fluorescence intensity profiles on day 7 (E), and C2C12 and NIH/3T3 spreading angle distributions on day 7 (F) of the MTU. The starting point of the fluorescence intensity profile was 0 and the end point was 1, which represented the longitudinal MTU interface. G) Schematic of the MMVU reconstructed by C2C12 myoblasts and HUVECs. H) C2C12 cells (green) and HUVECs (red) labeled with fluorescence tracers and vertically cryo-bioprinted as a MMVU model on day 7. I) Fluorescence microscopy images showing MMVU formation from days 1 to 7 after vertical 3D cryo-bioprinting. J–L) Quantification results of cell length from days 1 to 7 (J), fluorescence intensity profiles on day 7 (K), and C2C12 and NIH/3T3 spreading angle distribution on day 7 (L) of the MMVU after vertical 3D bioprinting. The starting point of the fluorescence intensity profile was 0 and the end point was 1, which represented the lateral MMVU interface (*$p < 0.05$).

ADVANCED
SCIENCE NEWS
www.advancedsciencenews.com

ADVANCED
MATERIALS
www.advmat.de

day 7 (Figure 6J), roughly matching those observed in the MTU experimentation. Similarly, the spreading area of the myotubes gradually increased following vertical cryo-bioprinting and subsequent culture. Finally, the fluorescence intensity profiles indicated that while the C2C12 cells and the HUVECs were separated in their respective filaments, they were closely arranged side-by-side showing signs of interactions and formation of the preliminary MMVU (Figure 6K). The orientation assessment of the C2C12 myoblasts and HUVECs in the filaments further validated that both of them were aligned perpendicular to the cross-sections of the filaments (Figure 6L).

3. Conclusion

We have developed an enabling vertical 3D cryo-bioprinting technique by combining extrusion bioprinting, directional freezing, and cryopreservation. Compared with traditional pure GelMA hydrogel scaffolds, vertically 3D-cryoprinted constructs allowed generation of controllable, anisotropic, interconnected microchannels, which presented enhanced mechanical properties. The flexibility of our technique was demonstrated by vertical cryoprinting of sophisticated structures, core–shell structures, and multimaterial structures. Contrary to conventional GelMA constructs, these vertically cryo-bioprinted constructs could increase cell activities and regulate cell behaviors, showing advantages in certain applications. For example, highly aligned myotubes were induced to form for the reconstruction of muscular tissues by embedding C2C12 myoblasts during the vertical cryo-bioprinting process. We could also successfully construct the MTU or the MMVU by co-cryo-bioprinting myoblasts with fibroblasts or endothelial cells consecutively or in parallel. It is hence rationally anticipated that our vertical 3D cryo-bioprinting strategy may find broad usage in engineering a variety of tissues that feature oriented internal cellular and ECM arrangements.

However, the technology is not without limitations. For example, the printing height would not be high enough to address some of the in vivo needs, which may require additional investigations. Another possible utility of the method lies in the creation of in vitro musculoskeletal models for biological studies, drug discovery, and personalized medicine, for which though, the size we are generating is more than sufficient. Further optimizations are also needed to customize the method based on the target tissues of interest, as well as more systematic in vivo investigations.

Supporting Information

Supporting Information is available from the Wiley Online Library or from the author.

Acknowledgements

Conflict of Interest

The authors declare no conflict of interest.

Data Availability Statement

The data that support the findings of this study are available from the corresponding author upon reasonable request.

[1] R. Levato, T. Jungst, R. G. Scheuring, T. Blunk, J. Groll, J. Malda, *Adv. Mater.* **2020**, *32*, 1906423.
[2] L. Moroni, J. A. Burdick, C. Highley, S. J. Lee, Y. Morimoto, S. Takeuchi, J. J. Yoo, *Nat. Rev. Mater.* **2018**, *3*, 21.
[3] S. V. Murphy, P. De Coppi, A. Atala, *Nat. Biomed. Eng.* **2020**, *4*, 370.
[4] M. A. Heinrich, W. Liu, A. Jimenez, J. Yang, A. Akpek, X. Liu, Q. Pi, X. Mu, N. Hu, R. M. Schiffelers, J. Prakash, J. Xie, Y. S. Zhang, *Small* **2019**, *15*, 1805510.
[5] Z. Liang, Y. Pei, C. Chen, B. Jiang, Y. Yao, H. Xie, M. Jiao, G. Chen, T. Li, B. Yang, L. Hu, *ACS Nano* **2019**, *13*, 12653.
[6] P. Zhuang, W. L. Ng, J. An, C. K. Chua, L. P. Tan, *PLoS One* **2019**, *14*, 0216776.
[7] S. Ostrovidov, S. Salehi, M. Costantini, K. Suthiwanich, M. Ebrahimi, R. B. Sadeghian, T. Fujie, X. Shi, S. Cannata, C. Gargioli, A. Tamayol, M. R. Dokmeci, G. Orive, W. Swieszkowski, A. Khademhosseini, *Small* **2019**, *15*, 1805530.
[8] Y. Jin, E. J. Jeon, S. Jeong, S. Min, Y. S. Choi, S. H. Kim, J. S. Lee, J. Shin, J. H. Yu, D.-H. Ahn, Y.-G. Kim, H. S. Yang, T. J. Kang, S.-R. Cho, N. Choi, S.-W. Cho, *Adv. Funct. Mater.* **2021**, *31*, 2006227.
[9] J. Zhang, Y. Chen, Y. Huang, W. Wu, X. Deng, H. Liu, R. Li, J. Tao, X. Li, X. Liu, M. Gou, *Adv. Sci.* **2020**, *7*, 2002601.
[10] G. Ying, N. Jiang, C. Parra-Cantu, G. Tang, J. Zhang, H. Wang, S. Chen, N.-P. Huang, J. Xie, Y. S. Zhang, *Adv. Funct. Mater.* **2020**, *30*, 2003740.
[11] G.-L. Ying, N. Jiang, S. Maharjan, Y.-X. Yin, R.-R. Chai, X. Cao, J.-Z. Yang, A. K. Miri, S. Hassan, Y. S. Zhang, *Adv. Mater.* **2018**, *30*, 1805460.
[12] H. Joukhdar, A. Seifert, T. Jüngst, J. Groll, M. S. Lord, J. Rnjak-Kovacina, *Adv. Mater.* **2021**, *33*, 2100091.
[13] A. Seifert, J. Groll, J. Weichhold, A. V. Boehm, F. A. Müller, U. Gbureck, *Adv. Eng. Mater.* **2021**, *23*, 2001417.
[14] A. Seifert, J. Gruber, U. Gbureck, J. Groll, *Adv. Eng. Mater.* **2021**, https://doi.org/10.1002/adem.202100860.
[15] K. Stuckensen, A. Schwab, M. Knauer, E. Muiños-López, F. Ehlicke, J. Reboredo, F. Granero-Moltó, U. Gbureck, F. Prósper, H. Walles, J. Groll, *Adv. Mater.* **2018**, *30*, 1706754.
[16] H. Bai, D. Wang, B. Delattre, W. Gao, J. De Coninck, S. Li, A. P. Tomsia, *Acta Biomater.* **2015**, *20*, 113.
[17] J. V. John, A. McCarthy, H. Wang, Z. Luo, H. Li, Z. Wang, F. Cheng, Y. S. Zhang, J. Xie, *Adv. Healthcare Mater.* **2021**, *10*, 2100238.
[18] H. Chang, S. W. T. Chew, M. Zheng, D. C. S. Lio, C. Wiraja, Y. Mei, X. Ning, M. Cui, A. Than, P. Shi, D. Wang, K. Pu, P. Chen, H. Liu, C. Xu, *Nat. Biomed. Eng.* **2021**, *5*, 1008.

[19] J. P. Rodrigues, F. H. Paraguassú-Braga, L. Carvalho, E. Abdelhay, L. F. Bouzas, L. C. Porto, *Cryobiology* **2008**, *56*, 144.

[20] T. Hino, M. Takabe, R. Suzuki-Migishima, M. Yokoyama, *Reprod. Med. Biol.* **2007**, *6*, 229.

[21] G. Shao, D. A. H. Hanaor, X. Shen, A. Gurlo, *Adv. Mater.* **2020**, *32*, 1907176.

[22] M. Hua, S. Wu, Y. Ma, Y. Zhao, Z. Chen, I. Frenkel, J. Strzalka, H. Zhou, X. Zhu, X. He, *Nature* **2021**, *590*, 594.

[23] X. Liang, G. Chen, S. Lin, J. Zhang, L. Wang, P. Zhang, Z. Wang, Z. Wang, Y. Lan, Q. Ge, J. Liu, *Adv. Mater.* **2021**, *33*, 2102011.

[24] M. C. Leu, B. K. Deuser, L. Tang, R. G. Landers, G. E. Hilmas, J. L. Watts, *CIRP Ann.* **2012**, *61*, 223.

[25] S. Ueno, R. Shirakashi, K.-i. Kudoh, T. Higuchi, G.-S. Do, T. Araki, Y. Sagara, *Biosci., Biotechnol., Biochem.* **2009**, *73*, 2478.

[26] S. Chen, T.-S. Jang, H. M. Pan, H.-D. Jung, M. W. Sia, S. Xie, Y. Hang, S. K. M. Chong, D. Wang, J. Song, *Int. J. Bioprint.* **2020**, *6*, 258.

[27] W. L. Ng, J. M. Lee, M. Zhou, Y.-W. Chen, K.-X. A. Lee, W. Y. Yeong, Y.-F. Shen, *Biofabrication* **2020**, *12*, 022001.

[28] Q. Pi, S. Maharjan, X. Yan, X. Liu, B. Singh, A. M. van Genderen, F. Robledo-Padilla, R. Parra-Saldivar, N. Hu, W. Jia, C. Xu, J. Kang, S. Hassan, H. Cheng, X. Hou, A. Khademhosseini, Y. S. Zhang, *Adv. Mater.* **2018**, *30*, 1706913.

[29] X. Cao, R. Ashfaq, F. Cheng, S. Maharjan, J. Li, G. Ying, S. Hassan, H. Xiao, K. Yue, Y. S. Zhang, *Adv. Funct. Mater.* **2019**, *29*, 1807173.

[30] L. Ouyang, C. B. Highley, W. Sun, J. A. Burdick, *Adv. Mater.* **2017**, *29*, 1604983.

[31] W. Liu, Z. Zhong, N. Hu, Y. Zhou, L. Maggio, A. K. Miri, A. Fragasso, X. Jin, A. Khademhosseini, Y. S. Zhang, *Biofabrication* **2018**, *10*, 024102.

[32] G. Tang, R. Xiong, D. Lv, R. X. Xu, K. Braeckmans, C. Huang, S. C. De Smedt, *Adv. Sci.* **2019**, *6*, 1802342.

[33] G. Tang, L. Chen, L. Lian, F. Li, H. Ravanbakhsh, M. Wang, Y. S. Zhang, C. Huang, *Chem. Eng. J.* **2021**, *407*, 127187.

[34] G. Tang, L. Chen, Z. Wang, S. Gao, Q. Qu, R. Xiong, K. Braeckmans, S. C. De Smedt, Y. S. Zhang, C. Huang, *Small* **2020**, *16*, 1907586.

[35] W. Liu, Y. S. Zhang, M. A. Heinrich, F. De Ferrari, H. L. Jang, S. M. Bakht, M. M. Alvarez, J. Yang, Y. C. Li, G. Trujillo-de Santiago, A. K. Miri, K. Zhu, P. Khoshakhlagh, G. Prakash, H. Cheng, X. Guan, Z. Zhong, J. Ju, G. H. Zhu, X. Jin, S. R. Shin, M. R. Dokmeci, A. Khademhosseini, *Adv. Mater.* **2018**, *29*, 1604630.

[36] J. Peng, A. P. Tomsia, L. Jiang, B. Z. Tang, Q. Cheng, *Nat. Commun.* **2021**, *12*, 4539.

[37] J. L. Chaytor, J. M. Tokarew, L. K. Wu, M. Leclere, R. Y. Tam, C. J. Capicciotti, L. Guolla, E. von Moos, C. S. Findlay, D. S. Allan, R. N. Ben, *Glycobiology* **2012**, *22*, 123.

[38] S. Ahn, H. Lee, E. J. Lee, G. Kim, *J. Mater. Chem. B* **2014**, *2*, 2773.

[39] T. K. Merceron, M. Burt, Y. J. Seol, H. W. Kang, S. J. Lee, J. J. Yoo, A. Atala, *Biofabrication* **2015**, *7*, 035003.

[40] M. E. Prendergast, M. D. Davidson, J. A. Burdick, *Biofabrication* **2021**, *13*, 044108.

[41] A. Kosik-Koziol, M. Costantini, T. Bolek, K. Szoke, A. Barbetta, J. Brinchmann, W. Swieszkowski, *Biofabrication* **2017**, *9*, 044105.

[42] S. Rathan, L. Dejob, R. Schipani, B. Haffner, M. E. Mobius, D. J. Kelly, *Adv. Healthcare Mater.* **2019**, *8*, 1801501.

[43] P. Zhuang, J. An, C. K. Chua, L. P. Tan, *Mater. Des.* **2020**, *193*, 108794.

[44] W. Kim, C. H. Jang, G. H. Kim, *Nano Lett.* **2019**, *19*, 8612.

[45] M. J. Mondrinos, F. Alisafaei, A. Y. Yi, H. Ahmadzadeh, I. Lee, C. Blundell, J. Seo, M. Osborn, T.-J. Jeon, S. M. Kim, V. B. Shenoy, D. Huh, *Sci. Adv.* **2021**, *7*, eabe9446.

[46] H. Hwangbo, H. Lee, E.-J. Jin, J. Lee, Y. Jo, D. Ryu, G. Kim, *Bioact. Mater.* **2022**, *8*, 57.

[47] B. Toprakhisar, A. Nadernezhad, E. Bakirci, N. Khani, G. A. Skvortsov, B. Koc, *Macromol. Biosci.* **2018**, *18*, 1800024.

[48] B. Bordoni, M. Varacallo, in *Anatomy, Tendons*, StatPearls Publishing, Treasure Island, FL, USA **2021**.

[49] C. Latroche, C. Gitiaux, F. Chrétien, I. Desguerre, R. Mounier, B. Chazaud, *Physiology* **2015**, *30*, 417.

[50] J. Koffler, K. Kaufman-Francis, Y. Shandalov, D. Egozi, D. A. Pavlov, A. Landesberg, S. Levenberg, *Proc. Natl. Acad. Sci. USA* **2011**, *108*, 14789.

[51] S. Levenberg, J. Rouwkema, M. Macdonald, E. S. Garfein, D. S. Kohane, D. C. Darland, R. Marini, C. A. van Blitterswijk, R. C. Mulligan, P. A. D'Amore, R. Langer, *Nat. Biotechnol.* **2005**, *23*, 879.

[52] Y. Shandalov, D. Egozi, J. Koffler, D. Dado-Rosenfeld, D. Ben-Shimol, A. Freiman, E. Shor, A. Kabala, S. Levenberg, *Proc. Natl. Acad. Sci. USA* **2014**, *111*, 6010.